Eur. Phys. J. D (2021) 75:190
https://doi.org/10.1140/epjd/s10053-021-00201-9

THE EUROPEAN PHYSICAL JOURNAL D

Regular Article - Ultraintense and Ultrashort Laser Fields

Edge-state influence on high-order harmonic generation in topological nanoribbons

Hannah Jürß[1,a] and Dieter Bauer[1,b]

[1] Institute of Physics, University of Rostock, 18051 Rostock, Germany

Received 26 March 2021 / Accepted 14 June 2021 / Published online 29 June 2021

Abstract. The high-order harmonic generation in finite topological nanoribbons is investigated using a tight-binding approximation. The narrow, two-dimensional ribbons consist of hexagonal structures. A topological phase transition is defined by a sudden change of the topological invariant. In the bulk, this kind of phase transition might occur if an existing band gap closes and reopens again. Through the bulk-boundary correspondence, this is related to the emergence of topologically protected edge states in the respective finite systems. For the finite ribbons studied in this work, the variation of the tight-binding parameters leads to the emergence of two edge states after the closing of the band gap. The energies of those edge states as functions of the tight-binding parameters display crossings and avoided crossings, which influence the high-harmonic spectra.

1 Introduction

Topological insulators are a special kind of solid-state material that is an electrical insulator in its bulk but conducting on its edges or surfaces. The edge or surface states are protected against perturbations [1]. The first realization of a topological insulator in the experiment was reported by König et al. in 2007 [2] using HgTe quantum wells. Topological insulators might play a big role in the development of quantum computers [1,3].

Recent studies show that the topological phase of a solid can have a huge influence on the generation of high-order harmonic radiation. In fact, the topological phase might affect the harmonic yield by several orders of magnitude [4–6], flip the helicity of the emitted photons [7–9] or introduce circular dichroism [10]. In three-dimensional topological insulators, the harmonic yield of bulk and surface states show a different dependency on the ellipticity of the laser field [11].

It is known that the high-harmonic generation (HHG) in solids in general carries information about the static and dynamic properties of the solid [12–17]. In this work, we investigate two-dimensional, hexagonal nanoribbons that are narrow, i.e., the ribbons are much longer in one of the two dimensions. The systems are described using a tight-binding approximation where hopping between nearest neighbors are allowed, thus describing graphene ribbons. The HHG in graphene was studied previously, for example in Refs. [18–21]. Adding an alternating on-site potential because of different atomic elements such as in hexagonal boron nitride (h-BN), for instance, the sublattice symmetry is broken. HHG in h-BN has been studied as well, e.g., in Refs. [22–24]. The dependence of HHG on the on-site potential for hexagonal ribbons was studied in [25,26].

With a broken time-reversal symmetry, the system might become topologically non-trivial. This can be achieved by including a complex hopping between next-nearest neighbors as in the Haldane-model [27]. The Haldane-model in the context of HHG was studied in Refs. [7,8,10].

In this paper, we examine how the edge states of Haldane nanoribbons influence the emission of high-order harmonics. Topological nanoribbons were studied without an external field in Ref. [28]. Although edge states are only present in finite systems, the bulk-boundary correspondence [29] tells that a non-vanishing difference between the topological invariants of the bands for the bulk imply the presence of edge states in the respective finite system. The question then is which topological effects in HHG spectra are due to bulk already and which require the explicit presence of edge states. An example system where the explicit presence of edge states is necessary to see any topological effect in HHG spectra is the one-dimensional Su-Schrieffer-Heeger chain [9]. In 2D systems such as the Haldane model, on the other hand, one can observe helicity flips already for bulk only [7,9].

The outline of the paper is as follows. In Sec. 2, we summarize the theoretical methods used in this work. In Sec. 3.1, the properties of the static system are explained, with a focus on the edge states. The HHG of Haldane nanoribbons is discussed in Sec. 3.2. If not

[a] e-mail: hannah.juerss@uni-rostock.de (corresponding author)
[b] e-mail: dieter.bauer@uni-rostock.de

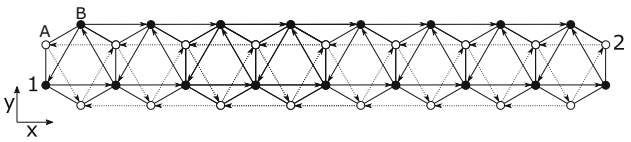

Fig. 1 Sketch of a nanoribbon with zigzag edges comprising eight hexagons. The circles indicate the atomic sites. The on-site potential on sites with an unfilled circle is given by M (sublattice A), and for the filled circles, it is given by $-M$ (sublattice site B). Lines (without arrow) indicate the hopping between nearest neighbors (amplitude t_1). The arrows indicate the next-nearest neighbor hopping with amplitude $\mathrm{i}t_2$ in the direction of the arrow (and $-\mathrm{i}t_2$ in the opposite direction). We label the lower left edge site '1' and the upper right edge site'2'

stated otherwise, atomic units (a.u., $\hbar = |e| = m_e = 4\pi\epsilon_0 = 1$) are used throughout this paper.

2 Theory

The systems that are investigated in this work are hexagonal ribbons with zigzag edges as shown in Fig. 1. The simulated ribbons consist of 30 hexagons though (not only eight, as shown in Fig. 1). A tight-binding approximation is used. The circles in Fig. 1 indicate the sites with an on-site potential M $(-M)$ for the unfilled (filled) circles, corresponding to the two sublattice sites A (unfilled) and B (filled). Lines without arrows indicate hopping between the nearest neighboring sites with an amplitude $t_1 \in \mathbb{R}$. The arrows indicate a complex next-nearest neighbor hopping with amplitude $\mathrm{i}t_2$ (with $t_2 \in \mathbb{R}$) along the arrows (and $-\mathrm{i}t_2$ in the opposite direction). The complex next-nearest neighbor hopping breaks the time-reversal symmetry, making the system topologically nontrivial for sufficiently large t_2 [27]. In this work, we will vary t_2.

Note, the hopping parameter t_2 cannot be influenced in a solid and is given by the system itself. However, the topological phase might be controlled by the complex phase of the hopping amplitude (here fixed to $\mathrm{e}^{\mathrm{i}\varphi_{t_2}} = \mathrm{i}$) or by the sub-cycle structure of non-resonant external fields [30]. Topological phase transitions are easier to control on synthetic platforms like waveguides [31] or cold atoms [32] but there is no HHG in these topological systems.

2.1 Static system

The theoretical description of the topological ribbons is almost the same as in Ref. [8], with the difference that periodic boundary conditions were assumed there. As a consequence, the hopping elements from the left to the right edge of the ribbon are missing in the present work.

The Hamiltonian describing the electrons on the ribbon reads in tight-binding approximation

$$\hat{H}_0 = t_1 \sum_{<i,j>} \left(|j\rangle\langle i| + \text{h.c.}\right) + \mathrm{i}\,t_2 \sum_{\ll i,j\gg} \left(|j\rangle\langle i| - \text{h.c.}\right) + M\left(\sum_{i\in A}|i\rangle\langle i| - \sum_{i\in B}|i\rangle\langle i|\right) \tag{1}$$

where the sums $\sum_{<i,j>}$ and $\sum_{\ll i,j\gg}$ run over all nearest and next-nearest neighboring sites i, j, respectively. The sum $\sum_{i\in A}$ $(\sum_{i\in B})$ include all sites on sublattice site A (B). The state $|i\rangle$ denotes the atomic orbital at site i. A general state reads

$$|\psi\rangle = \sum_{i=1}^{N} g_i\,|i\rangle\,, \tag{2}$$

where N is the number of sites in the system.

The time-independent Schrödinger equation

$$\hat{H}_0\,|\psi_l\rangle = E_l\,|\psi_l\rangle \tag{3}$$

is solved to obtain the eigenstates $|\psi_l\rangle$ with their respective energies E_l. The number of eigenstates is given by the number of sites N, i.e., $l = 0, 1, 2, ..., N-1$. The labeling is such that the energies of the states increase with l, i.e., $E_0 \le E_1 \le E_2 \le ... \le E_{N-1}$. Equation (3) is solved numerically by diagonalization of the Hamiltonian (1).

The distance between nearest neighbors is set to $a = 2.68\,\text{a.u.} \simeq 1.42\,\text{Å}$ and the hopping between them to $t_1 = -0.1$ a.u. $\simeq -2.7\,\text{eV}$, the parameters for graphene [33]. The on-site potential M and the next-nearest neighbor hopping amplitude t_2 are varied in this work.

2.2 Coupling to an external field

The ribbons are coupled to an external field via velocity gauge, which translates to the Peierls substitution [34] in tight-binding approximation. The gauge-invariant coupling of general tight-binding systems to external fields was derived in Ref. [35].

The laser pulses are described by a vector potential of the form

$$\boldsymbol{A}(t) = A_0\,\sin^2\left(\frac{\omega_0 t}{2n_0}\right)\,\sin(\omega_0 t)\boldsymbol{e}_x, \tag{4}$$

for times $0 \le t \le 2\pi n_0/\omega_0$ (and zero otherwise). It is linearly polarized along the ribbon, that is, in x-direction. The number of cycles in the laser pulse is chosen $n_0 = 5$, the amplitude of the vector potential $A_0 = 0.05$ (intensity $\simeq 5\times10^9$ Wcm^{-2}), and the angular frequency is $\omega_0 = 7.5\cdot10^{-3}$ (i.e., wavelength $\lambda_0 = 6.1\mu\text{m}$).

We assume that all states with an energy smaller than $E = 0$ are occupied. Due to the symmetry of the energy spectrum, these are half of the states. Hence, $|\Psi_l(t)\rangle$ with $l = 0, 1, 2, ..., N/2 - 1$ are propagated in time, starting from $|\Psi_l(t = 0)\rangle = |\psi_l\rangle$.

The total current is given by

$$\boldsymbol{J}(t) = \sum_{l=0}^{N/2-1} \langle \Psi^l(t) | \hat{\boldsymbol{j}}(t) | \Psi^l(t) \rangle , \tag{5}$$

where the current operator is given by [36]

$$\hat{\boldsymbol{j}}(t) = -\mathrm{i} \sum_{i,j} (\boldsymbol{r}_i - \boldsymbol{r}_j) |i\rangle \langle i| \hat{H}(t) |j\rangle \langle j| , \tag{6}$$

with the positions $\boldsymbol{r}_{i,j}$ of sites i, j. The time-dependent Hamiltonian reads

$$\langle i| \hat{H}(t) |j\rangle = \langle i| \hat{H}_0 |j\rangle \, \mathrm{e}^{-\mathrm{i}(\boldsymbol{r}_i - \boldsymbol{r}_j)\cdot \boldsymbol{A}(t)}. \tag{7}$$

Harmonic spectra are calculated from the two components of the current (5) via a Fourier transformation,

$$P_{\parallel,\perp}(\omega) = \int_{-\infty}^{+\infty} \dot{J}_{x,y}(t) \, \mathrm{e}^{-\mathrm{i}\omega t} \mathrm{d}t. \tag{8}$$

Here, $\parallel$ and $\perp$ denote the polarization direction of the emitted light with respect to the incoming field: parallel (x-direction) and perpendicular (y-direction), respectively. In the code, the Fourier transformation is approximated by the fast Fourier transformation. The functions $\left|P_{\parallel,\perp}(\omega)\right|^2$ are proportional to the intensity of the emitted light [37–39] polarized in the respective direction. The phase difference

$$\Delta\phi = \arg\left(P_{\parallel}(\omega) P_{\perp}^*(\omega)\right) \tag{9}$$

indicates the helicity of the emitted photons.

3 Results

3.1 Static system

The number of atoms and eigenstates for the 30-hexagon long ribbons is $N = 122$. In Fig. 2, the energies of all states as function of the next-nearest neighbor hopping amplitude t_2 are shown for $M = 0$ (Fig. 2a) and $M = 0.01$ (Fig. 2b). For $M = 0$ (Fig. 2a), a band gap opens as t_2 increases so that the fully occupied valence band with $E < 0$ and the empty conduction band with $E > 0$ become well-separated. In the middle of the gap, two states appear around an energy of $E = 0$. One of this state is occupied, the other one not. For the system with an on-site potential of $M = 0.01$ (Fig. 2b), there is already a band gap for $t_2 = 0$ but without states in the middle. First, this band gap closes

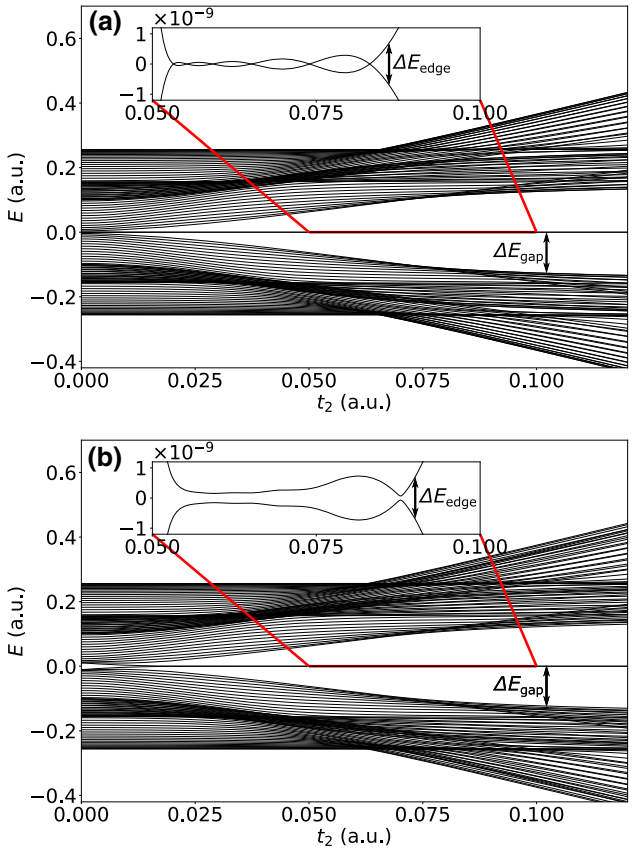

Fig. 2 Energies of the system for **a** $M = 0$ and **b** $M = 0.01$ as function of t_2. The insets show the evolution of the two states in a tiny energy interval around $E = 0$

with increasing t_2 before it opens up again for larger values. This band gap closure is an indication for a topological phase transition. In fact, in the middle of the band gap two states appear when the band gap opens up again. We will call those two states edge states because their probability density is located on the edges of the chain, as shown in Fig. 4. We define the energy difference ΔE_{gap} as the energy difference between the valence band and the lowest edge state energy.

The insets in Figs. 2a,b are magnifications and show the tiny energies of both edge states between $0.05 \leq t_2 \leq 0.01$. Their difference is defined as ΔE_{edge}. Surprisingly, the energies of these states do not just monotonically converge to $E = 0$. For $M = 0$, they cross six times in the interval shown before their energies separate for larger t_2. For the finite on-site potential in Fig. 2b, the crossings turn into avoided crossings.

In Fig. 3, the energy difference between the edge states ΔE_{edge} is shown for different M as function of t_2. It shows the crossings for $M = 0$ and that these crossings become avoided crossings for larger M. As the on-site potential increases further, the avoided crossings tend to smooth out. For $M = 0.01$ and $M = 0.02$, there are mainly two local minima. The energy difference ΔE_{edge} decreases with t_2 up to a local minimum at around $t_2 = 0.059$ for $M = 0.01$. The slope of ΔE_{edge}

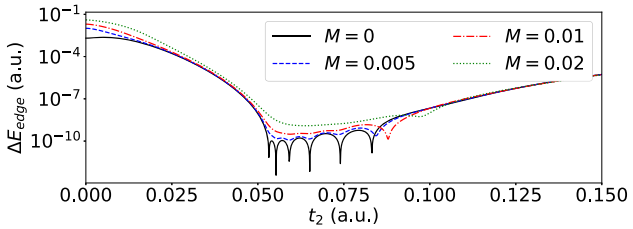

Fig. 3 Energy difference between the edge states as function of t_2 on a logarithmic scale for different on-site potentials M

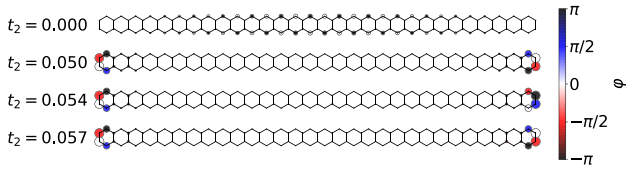

Fig. 4 Wave function of the highest occupied state (lowest state of the two edge states) for $M = 0$ and different t_2. The size of the circles indicates the probability density. The phase of the wave function is indicated by the color of the circles

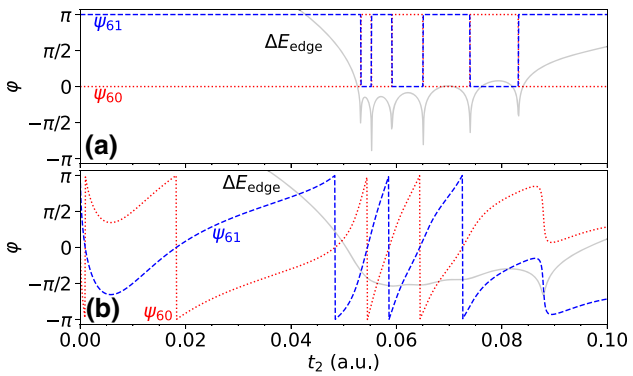

Fig. 5 Phase of the wave function of the initially highest occupied state (Ψ_{60}) and the lowest unoccupied state (Ψ_{61}) on site 2 (see Fig. 1) of the ribbon as function of t_2 for an on-site potential $M = 0$ (a) and $M = 0.01$ (b). The differences of the energies of both states ΔE_{edge} on a logarithmic scale from Fig. 3 are included in gray to show that phase jumps occur at (avoided) crossings

following this local minimum is quite shallow, rendering it a flat local minimum. A much more localized minimum occurs at $t_2 = 0.088$. Both minima are shifted toward larger t_2 as M increases. The other crossings cannot be observed anymore as the on-site potential becomes larger.

In Fig. 4, the wave function ψ_{60} of the state within the band gap with the smaller energy is shown. This is the highest, initially occupied state. The size of the sketched circles at the lattice site scales with the probability density there. The phase of the wave function is indicated by the color of the circles. For ease of comparison, we use a phase convention for the initial states for which the phase at site 1 is zero (see Fig. 1). The wave functions are given for different t_2 but fixed on-site potential $M = 0$. For $t_2 = 0$ the probability density is equally located on the upper and lower edge. With increasing t_2, the electron probability moves toward the left and right edges. The same happens for the lowest unoccupied state ψ_{61}, whose phase is different but probability density is the same (not shown). Because of the dominant location of the electron at the edges, we call these two states edge states. Clearly, for a system periodic in x-direction, these kind of states are absent due to the absence of left and right edges.

Crossings of the energies between both edge states occur at $t_2 = 0.053$ and $t_2 = 0.055$. For $t_2 = 0.05$, one can see a certain symmetry of the highest occupied state in Fig. 4. The phases of the wave function at the four leftmost sites, reading from top to bottom, is identical to the phases at the four rightmost sites but reading from bottom to top. The electron is mainly located on those eight sites. The wave function is symmetric under rotation by 180° about an axis perpendicular to the xy-plane of the ribbon and through its center. For $t_2 = 0.054$, the energies of both edge states have crossed so that the occupied state should now have the properties of the (for lower t_2) unoccupied one, and the other way around. Indeed, the phases of the wave function on the right edge of state ψ_{60} are now different. The state is not symmetric anymore under rotations by 180°. The phases at the four rightmost sites reading, from bottom to top, is identical to the phase at the four leftmost sites, read from top to bottom, plus π. This is indeed the symmetry of the other edge state. The next crossing appears at $t_2 = 0.055$. The symmetry of the highest occupied state for $t_2 = 0.057$ is now identical to the state for $t_2 = 0.05$, indicating that another crossing occurred.

In order to identify the exchange of the edge states, it is sufficient to look at the phases at, e.g., site 2 (see Fig. 1). In Fig. 5, the phase at this site for both edge states ψ_{60} and ψ_{61} is shown as function of t_2. In Fig. 5a, the phases for $M = 0$ are shown. The phases are constant for small t_2. For the highest occupied state ψ_{60}, the phase is $\varphi = 0$ and $\varphi = \pi$ for the lowest unoccupied state ψ_{61}. At each crossing, the phases of both states change to the value of the other state, indicating that the properties of both states are exchanged each time their energies cross. In order to remind for which t_2 crossings occur, the energy difference ΔE_{edge} from Fig. 3 is sketched in gray. In Fig. 5b, the same is plotted for an on-site potential of $M = 0.01$. From a local minimum at $t_2 = 0.0058$, both phases increase up to $t_2 = 0.088$ where ΔE_{edge} assumes a minimum. (Note that we plot phases modulo 2π within the interval $[-\pi, \pi)$ so that phases exceeding π reenter at $-\pi$.) In a narrow neighborhood around this value of t_2, both phases change by about π in a continuous manner, which is characteristic of an avoided crossing. The properties of the two edge states also exchange in this case so that the previously highest occupied state becomes the previously lowest unoccupied state and the other way around.

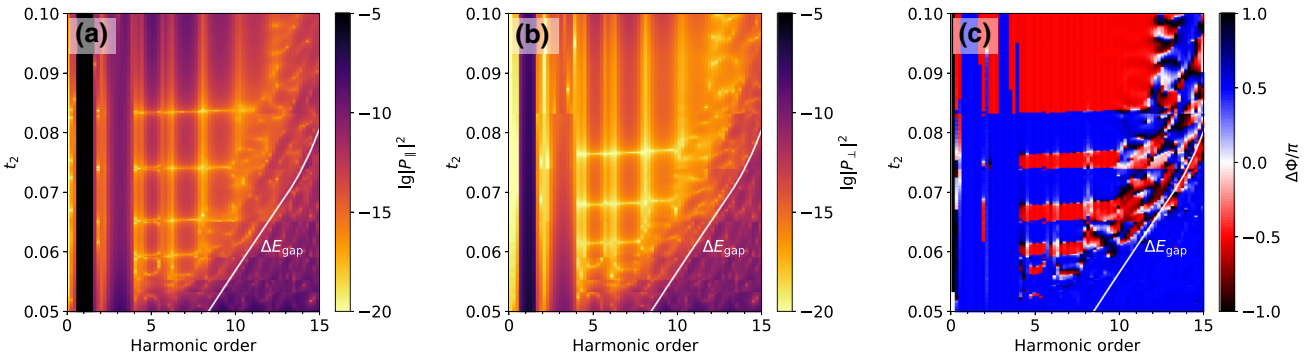

Fig. 6 High-order harmonic spectrum in **a** parallel and **b** perpendicular direction to the polarization of the external field, and **c** the corresponding phase difference between both components as a contour plot as function of t_2. The on-site potential is $M = 0.0$. The white line ΔE_{gap} is the gap between the valence band and the lowest edge state

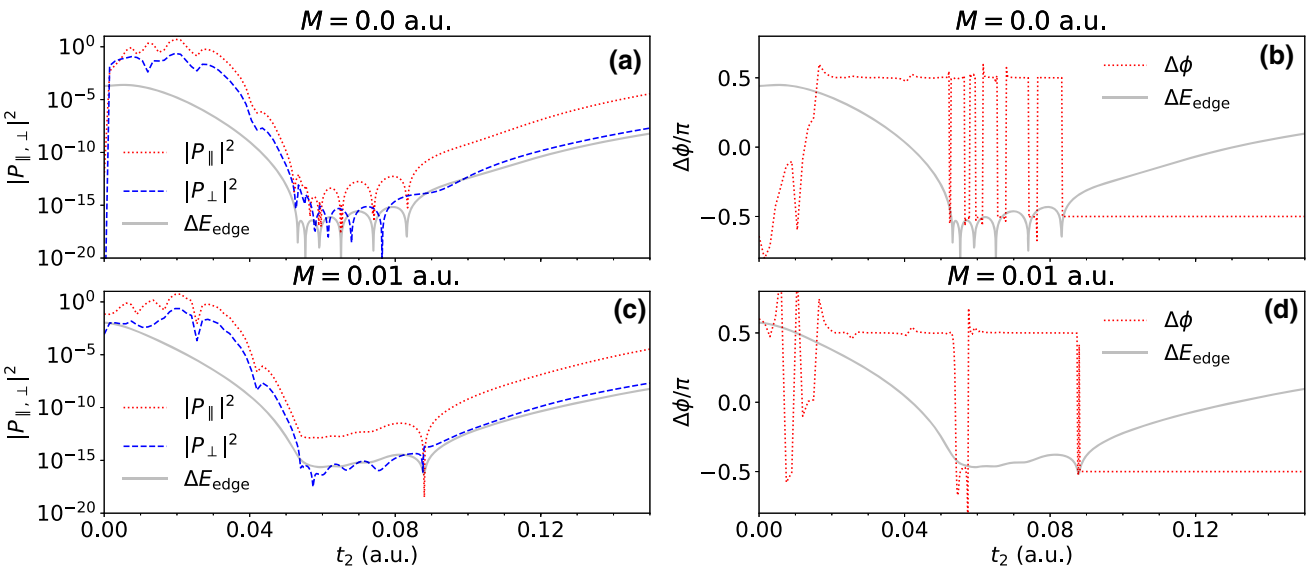

Fig. 7 Harmonic yield for both polarization directions **a**, **c**) and phase difference **b**, **d** for harmonic order 5 as function of t_2. For **a**, **b**, the on-site potential is $M = 0$, for **c**, **d** $M = 0.01$. The energy difference ΔE_{edge} is included in gray to ease the interpretation of the results (extra y-axis for ΔE_{edge} suppressed)

3.2 High-harmonic generation

Figure 6 shows harmonic spectra in parallel (Fig. 6a) and perpendicular (Fig. 6b) polarization direction to the polarization of the incoming field for $M = 0$ as function of t_2. In Fig. 6c, the phase difference (9) between both components is shown. Just to avoid confusion, in the previous sections, we discussed phases of electronic edge states φ, and now we examine the phases of the emitted harmonic radiation $\Delta\phi$. The goal is to understand how both are related.

We only show the spectra for the parameter space where the properties of the edge states matter. For more details at other parameters, in particular higher harmonic orders, we refer to Ref. [8]. The harmonics of interest are below energy ΔE_{gap}, which is defined by the highest state of the valence band and the lowest edge state (see Fig.2). The harmonic yield in this region decreases exponentially with harmonic order due to the destructive interference of intraband harmonics [4]. However, odd harmonics can still be observed up to order 9 or 11, depending on t_2. At certain t_2, the harmonic yield drops drastically for harmonics 5 till 9. This can be seen as a yellow horizontal traces in Figs. 6a,b. In the phase plot, several flips of the phase from blue to red color (flip by $\pm\pi$) can be observed. For a fixed harmonic order (5 till 9), the phase difference flips several times as t_2 increases.

In Fig. 7, the harmonic yield in both polarization directions for harmonic order 5 is shown for $M = 0$ (Fig. 7a) and $M = 0.01$ (Fig. 7c) as function of t_2. The respective phase differences (9) are shown in Fig. 7b ($M = 0$) and Fig. 7d ($M = 0.01$). The energy difference of the edge states ΔE_{edge} is included (with an extra y-axis suppressed, as only the behavior as function of t_2 is relevant).

In Fig. 7a, one can see a decreased harmonic yield in parallel polarization direction that occurs exactly at the

points where ΔE_{edge} is minimal (crossing of the edge states). There is an exception for the first two local minima of ΔE_{edge} where no significant decrease in the harmonic yield is observed. The minima of the yield in the perpendicular direction are located between two crossings (again with an exception between the first two crossings). In the phase difference (Fig. 7b), a phase flip from $\Delta\phi = \pi/2$ to $\Delta\phi = -\pi/2$ can be observed for the last four crossings. The phase flips back to $\Delta\phi = \pi/2$ between two crossing points. The back-flip of the phase is located at about the local minima of the yield in perpendicular polarization direction. Interestingly, the phase difference is $\Delta\phi = \pi/2$ before the first crossing and becomes $\Delta\phi = -\pi/2$ after the last crossing point. Further, we note that the harmonic yield in parallel polarization direction is related to ΔE_{edge} for sufficiently large t_2 ($t_2 > 0.055$).

In Figs. 7c and 7d, the harmonic yield and the phase difference is shown for $M = 0.01$. The harmonic yield in parallel polarization direction drops again drastically at the local minimum of ΔE_{edge} at $t_2 = 0.088$. This is the point where the energies of the edge states have an avoided crossing. The harmonic yield in perpendicular direction drops at the same value but not as much as the yield in parallel direction. Before the first local minimum of ΔE_{edge}, the phase difference is fluctuating around vales $\Delta\phi = \pi/2$. At the first local minimum at $t_2 = 0.059$, a phase flip to $\Delta\phi = -\pi/2$ can be observed but the phase flips back to $\Delta\phi = \pi/2$ for a slightly larger t_2. At the point of the avoided crossing at $t_2 = 0.088$, the phase flips permanently to $\Delta\phi = -\pi/2$.

The two graphs of the phase difference Figs. 7b,d show that the (avoided) crossings of the edge state energies cause a phase flip by π. Between two crossings, the phase flips back slightly after the first of the two crossings. Comparing the phases for small and large t_2, the phase changes from $\Delta\phi = \pi/2$ (small t_2) to $\Delta\phi = -\pi/2$ (large t_2).

The phase flips at the crossing points can be understood by the edge states. The properties of the initially occupied and unoccupied edge state exchange at each crossing point (and the avoided crossing at $t_2 = 0.088$ for $M = 0.01$). Therefore, the occupied edge state suddenly has the symmetry of the unoccupied state and the other way around. This affects the yield and the helicity of the emitted harmonics, as just demonstrated.

In the parameter regime where the phase flips occur, the harmonic yield for both polarization directions differs several orders of magnitude for fixed t_2. This means that despite $\Delta\phi = \pm\pi/2$, the ellipticity of the emitted harmonics is close to zero, i.e., the harmonics are almost linearly polarized. Nevertheless, the helicity flips discussed in this work should be measurable experimentally by interferometric means.

4 Summary and outlook

The edge states in the simulated finite, topological nanoribbons show a specific behavior as the tight-binding parameters are varied. The two edge states do not converge to the same energy but show crossings and avoided crossings. These crossings have a significant influence on the harmonic generation process. The phase difference between the two polarization components of the emitted light for certain harmonic orders change where the edge state energies cross (or have an avoided crossing). We find that the yield of low-order harmonics polarized parallel to the polarization of the incoming field is related to the energy difference of the edge states.

Certainly, our model studies presented in this work are highly idealized and simplified, as is the original Haldane model for the corresponding bulk. However, tailorable anomalous Hall systems are available (see, e.g., [40] and references therein), and a more realistic theoretical description of HHG in such systems is worthwhile to pursue in future work.

Acknowledgements H.J. acknowledges financial support by the doctoral fellowship program of the University of Rostock.

Author contributions

H.J. performed the numerical simulations, analyzed the results, and wrote the manuscript. D.B. provided critical feedback, supported the analysis of the results, and improved the final version of the manuscript.

Funding Open Access funding enabled and organized by Projekt DEAL.

Data availibility This manuscript has no associated data or the data will not be deposited. [Authors' comment: The data that support the findings of this study are available on request from the author H.J.]

References

1. M.Z. Hasan, C.L. Kane, Colloquium: Topological insulators. Rev. Mod. Phys. **82**, 3045–3067 (2010)

2. M. König, S. Wiedmann, C. Brüne, A. Roth, H. Buhmann, L.W. Molenkamp, X.-L. Qi, S.-C. Zhang, Quantum Spin Hall Insulator State in HgTe Quantum Wells. Science **318**(5851), 766–770 (2007)
3. J.E. Moore, The birth of topological insulators. Nature **464**, 194–198 (2010)
4. D. Bauer, K.K. Hansen, High-harmonic generation in solids with and without topological edge states. Phys. Rev. Lett. **120**, 177401 (2018)
5. H. Drüeke, D. Bauer, Robustness of topologically sensitive harmonic generation in laser-driven linear chains. Phys. Rev. A **99**, 053402 (2019)
6. H. Jürß, D. Bauer, High-harmonic generation in Su-Schrieffer-Heeger chains. Phys. Rev. B **99**, 195428 (2019)
7. R.E.F. Silva, Á. Jiménez-Galán, B. Amorim, O. Smirnova, M. Ivanov, Topological strong-field physics on sub-laser-cycle timescale. Nat. Photonics **13**, 849–854 (2019)
8. H. Jürß, D. Bauer, Helicity flip of high-order harmonic photons in Haldane nanoribbons. Phys. Rev. A **102**, 043105 (2020)
9. D. Moos, H. Jürß, D. Bauer, Intense-laser-driven electron dynamics and high-order harmonic generation in solids including topological effects. Phys. Rev. A **102**, 053112 (2020)
10. A. Chacón, D. Kim, W. Zhu, S.P. Kelly, A. Dauphin, E. Pisanty, A.S. Maxwell, A. Picón, M.F. Ciappina, D.E. Kim, C. Ticknor, A. Saxena, M. Lewenstein, Circular dichroism in higher-order harmonic generation: Heralding topological phases and transitions in Chern insulators. Phys. Rev. B **102**, 134115 (2020)
11. D. Baykusheva, A. Chacón, D. Kim, D.E. Kim, D.A. Reis, S. Ghimire, Strong-field physics in three-dimensional topological insulators. Phys. Rev. A **103**, 023101 (2021)
12. G. Vampa, T.J. Hammond, N. Thiré, B.E. Schmidt, F. Légaré, C.R. McDonald, T. Brabec, D.D. Klug, P.B. Corkum, All-optical reconstruction of crystal band structure. Phys. Rev. Lett. **115**, 193603 (2015)
13. M. Hohenleutner, F. Langer, O. Schubert, M. Knorr, U. Huttner, S.W. Koch, M. Kira, R. Huber, Real-time observation of interfering crystal electrons in high-harmonic generation. Nature **523**, 572–575 (2015)
14. T.T. Luu, M. Garg, S.Y. Kruchinin, A. Moulet, M.T. Hassan, E. Goulielmakis, Extreme ultraviolet high-harmonic spectroscopy of solids. Nature **521**, 498–502 (2015)
15. G. Vampa, T. Brabec, Merge of high harmonic generation from gases and solids and its implications for attosecond science. J. Phys. B: At. Mol. Opt. Phys. **50**, 083001 (2017)
16. Y.S. You, Y. Yin, Y. Wu, A. Chew, X. Ren, F. Zhuang, S. Gholam-Mirzaei, M. Chini, Z. Chang, S. Ghimire, High-harmonic generation in amorphous solids. Nat. Commun. **8**, 724 (2017)
17. M. Baudisch, A. Marini, J.D. Cox, T. Zhu, F. Silva, S. Teichmann, M. Massicotte, F. Koppens, L.S. Levitov, F.J. García de Abajo, J. Biegert, Ultrafast nonlinear optical response of Dirac fermions in graphene. Nat. Commun. **9**, 1018 (2018)
18. D. Dimitrovski, L.B. Madsen, T.G. Pedersen, High-order harmonic generation from gapped graphene: Perturbative response and transition to nonperturbative regime. Phys. Rev. B **95**, 035405 (2017)
19. L.A. Chizhova, F. Libisch, J. Burgdörfer, High-harmonic generation in graphene: Interband response and the harmonic cutoff. Phys. Rev. B **95**, 085436 (2017)
20. N. Yoshikawa, T. Tamaya, K. Tanaka, High-harmonic generation in graphene enhanced by elliptically polarized light excitation. Science **356**, 736–738 (2017)
21. H.A. Hafez, S. Kovalev, J.-C. Deinert, Z. Mics, B. Green, N. Awari, M. Chen, S. Germanskiy, U. Lehnert, J. Teichert, Z. Wang, K.-J. Tielrooij, Z. Liu, Z. Chen, A. Narita, K. Müllen, M. Bonn, M. Gensch, D. Turchinovich, Extremely efficient terahertz high-harmonic generation in graphene by hot Dirac fermions. Nature **561**, 507–511 (2018)
22. N. Tancogne-Dejean and A. Rubio, "Atomic-like high-harmonic generation from two-dimensional materials," *Science Advances*, vol. 4, Feb 2018
23. G. Le Breton, A. Rubio, N. Tancogne-Dejean, High-harmonic generation from few-layer hexagonal boron nitride: Evolution from monolayer to bulk response. Phys. Rev. B **98**, 165308 (2018)
24. L. Yue, M.B. Gaarde, Structure gauges and laser gauges for the semiconductor Bloch equations in high-order harmonic generation in solids. Phys. Rev. A **101**, 053411 (2020)
25. H. Jürß and D. Bauer, "High-order harmonic generation in hexagonal nanoribbons," *The European Physical Journal Special Topics*, Apr 2021
26. H. Drüeke, D. Bauer, "High-harmonic spectra of hexagonal nanoribbons from real-space timedependent Schrödinger calculations," Eur. Phys. J. Spec. Top. (2021). https://doi.org/10.1140/epjs/s11734-021-00188-9
27. F.D.M. Haldane, Model for a Quantum Hall Effect without Landau Levels: Condensed-Matter Realization of the "Parity Anomaly". Phys. Rev. Lett. **61**, 2015–2018 (1988)
28. N. Hao, P. Zhang, Z. Wang, W. Zhang, Y. Wang, Topological edge states and quantum Hall effect in the Haldane model. Phys. Rev. B **78**, 075438 (2008)
29. J. Asbóth, L. Oroszlány, and A. Pályi, *A Short Course on Topological Insulators*, vol. 919 of *Lecture Notes in Physics*. Springer, 2016
30. Á. Jiménez-Galán, R.E.F. Silva, O. Smirnova, M. Ivanov, Lightwave control of topological properties in 2D materials for sub-cycle and non-resonant valley manipulation. Nat. Photonics **14**, 728–732 (2020)
31. M. C. Rechtsman, J. M. Zeuner, Y. Plotnik, Y. Lumer, D. Podolsky, F. Dreisow, S. Nolte, M. Segev, and A. Szameit, "Photonic floquet topological insulators," *Nature*, vol. 496, pp. 196 EP –, Apr 2013
32. N. Goldman, J. Dalibard, A. Dauphin, F. Gerbier, M. Lewenstein, P. Zoller, I.B. Spielman, Direct imaging of topological edge states in cold-atom systems. Proc. Natl. Acad. Sci. **110**(17), 6736–6741 (2013)
33. D. R. Cooper, B. D'Anjou, N. Ghattamaneni, B. Harack, M. Hilke, A. Horth, N. Majlis, M. Massicotte, L. Vandsburger, E. Whiteway, and V. Yu, "Experimental Review of Graphene," *ISRN Condensed Matter Physics*, vol. 2012, Apr 2012. Article ID 501686

34. R. Peierls, Zur Theorie des Diamagnetismus von Leitungselektronen. Zeitschrift für Physik **80**, 763–791 (1933)
35. M. Graf, P. Vogl, Electromagnetic fields and dielectric response in empirical tight-binding theory. Phys. Rev. B **51**, 4940–4949 (1995)
36. A. L. Kuzemsky, "Electronic transport in metallic systems and generalized kinetic equations," *International Journal of Modern Physics B*, vol. 25, no. 23n24, pp. 3071–3183, 2011
37. A.D. Bandrauk, S. Chelkowski, D.J. Diestler, J. Manz, K.-J. Yuan, Quantum simulation of high-order harmonic spectra of the hydrogen atom. Phys. Rev. A **79**, 023403 (2009)
38. J.C. Baggesen, L.B. Madsen, On the dipole, velocity and acceleration forms in high-order harmonic generation from a single atom or molecule. J. Phys. B: At. Mol. Opt. Phys. **44**, 115601 (2011)
39. D. Bauer, H. Bauke, T. Brabec, T. Fennel, C. R. McDonald, D. B. Milošević, S. Pabst, C. Peltz, G. Pöplau, R. Santra, and C. Varin, *Computational Strong-Field Quantum Dynamics: Intense Light-Matter Interactions*. De Gruyter Textbook, De Gruyter
40. C.-Z. Chen, Y.-M. Xie, J. Liu, P.A. Lee, K.T. Law, Quasi-one-dimensional quantum anomalous hall systems as new platforms for scalable topological quantum computation. Phys. Rev. B **97**, 104504 (2018)